Biomedical Optics EXPRESS

Aberrations and their correction in light-sheet microscopy: a low-dimensional parametrization

Diwakar Turaga and Timothy E. Holy*

Dept. of Anatomy & Neurobiology, Washington University in St. Louis School of Medicine, St. Louis, MO 63110, USA

**holy@wustl.edu*

Abstract: Light sheet microscopy allows rapid imaging of three-dimensional fluorescent samples, using illumination and detection axes that are orthogonal. For imaging large samples, this often forces the objective to be tilted relative to the sample's surface; for samples that are not precisely matched to the immersion medium index, this tilt introduces aberrations. Here we calculate the nature of these aberrations for a simple tissue model, and show that a low-dimensional parametrization of these aberrations facilitates online correction via a deformable mirror without introduction of beads or other fiducial markers. We use this approach to demonstrate improved image quality in living tissue.

OCIS codes: (110.1080) Active or adaptive optics; (180.2520) Fluorescence microscopy.

References and links

1. J. J. J. Dirckx, L. C. Kuypers, and W. F. Decraemer, "Refractive index of tissue measured with confocal microscopy," J. Biomed. Opt. **10**, 44014 (2005).
2. C. J. Sheppard and M. Gu, "Aberration compensation in confocal microscopy," Appl. Opt. **30**, 3563–3568 (1991).
3. J. Porter, H. M. Queener, J. E. Lin, K. Thorn, and A. Awwal, *Adaptive Optics for Vision Science* (Wiley, 2006).
4. P. A. Santi, "Light sheet fluorescence microscopy: a review," J. Histochem. Cytochem. **59**, 129–138 (2011).
5. T. F. Holekamp, D. Turaga, and T. E. Holy, "Fast three-dimensional fluorescence imaging of activity in neural populations by objective-coupled planar illumination microscopy," Neuron **57**, 661–672 (2008).
6. D. Turaga and T. E. Holy, "Organization of vomeronasal sensory coding revealed by fast volumetric calcium imaging," J. Neurosci. **32**, 1612–1621 (2012).
7. C. Bourgenot, C. D. Saunter, J. M. Taylor, J. M. Girkin, and G. D. Love, "3d adaptive optics in a light sheet microscope," Opt. Express **20**, 13252–13261 (2012).
8. R. Jorand, G. Le Corre, J. Andilla, A. Maandhui, C. Frongia, V. Lobjois, B. Ducommun, and C. Lorenzo, "Deep and clear optical imaging of thick inhomogeneous samples," PloS One **7**, e35795 (2012).
9. W. H. Press, S. A. Teukolsky, W. T. Vetterling, and B. P. Flannery, *Numerical Recipes in C++: The Art of Scientific Computing*, 3rd ed. (Cambridge University Press Cambridge, 2007).
10. D. Turaga and T. E. Holy, "Miniaturization and defocus correction for objective-coupled planar illumination microscopy," Opt. Lett. **33**, 2302–2304 (2008).
11. M. Born and E. Wolf, *Principles of Optics* (Pergamon Press, 1980), 6th ed.
12. J. L. F. de Meijere and C. H. F. Velzel, "Linear ray-propagation models in geometrical optics," J. Opt. Soc. Am. A **4**, 2162–2165 (1987).
13. D. Turaga and T. E. Holy, "Image-based calibration of a deformable mirror in wide-field microscopy," Appl. Opt. **49**, 2030–2040 (2010).
14. J. He, L. Ma, S. Kim, J. Nakai, and C. Yu, "Encoding gender and individual information in the mouse vomeronasal organ," Science **320**, 535–538 (2008).

#189627 - $15.00 USD Received 29 Apr 2013; revised 20 Jun 2013; accepted 30 Jun 2013; published 14 Aug 2013

1. Introduction

When imaging biological tissues by optical microscopy, image quality is degraded by both scattering and classical aberrations. The latter arise from changes in refractive index, either locally within the sample or at the interface between the sample and the immersion fluid. When examining living samples, the immersion fluid is typically saline, with a refractive index of approximately 1.34; most tissues have an average (bulk) refractive index in the range 1.36–1.40 [1]. Consequently, the saline/tissue interface is a significant source of aberration. Using traditional forms of microscopy, this interface is approximately perpendicular to the imaging axis; under these conditions, spherical aberration plays the dominant role [2, 3].

Recently, light sheet illumination microscopy has emerged as an attractive technique for rapid three-dimensional imaging [4]. In light sheet microscopy, the "axial" direction for imaging is orthogonal to the direction of propagation of the illumination. To image large samples, such as the mammalian nervous system [5, 6], it is therefore necessary to tilt the illumination and detection axes relative to the sample surface (Fig. 1). This tilt introduces new aberrations at the saline/tissue interface that are not significant when imaging tissue face-on. While both the illumination and detection paths are affected by these aberrations, their consequence is more serious for the detection path because of its higher numerical aperture. The detection aberrations have been corrected using wavefront sensors with beads as fiducial markers [7, 8] and/or via an image-based optimization of Zernike modes 4–15 [7]. However, both approaches have limitations: the introduction of beads into samples can be problematic in practice, and optimization of image quality in a 12-dimensional space requires extensive search and collection of many calibration images. In particular, gradient-free optimization of even a simple quadratic function of N variables typically takes $O(N^2)$ iterations [9]; during correction with 12 parameters, many trial images have to be collected and, in the presence of noise, it may be difficult to assess progress in searching such a high-dimensional space. Under normal imaging conditions, these considerations may serve as an obstacle to achieving large improvements in image quality [7, Fig. 6].

Here we use a perturbative approach to calculate the low-order aberrations that arise from imaging at a tilt through a refractive index mismatch. We show that the aberration structure can be described using just two or three parameters. This low-dimensional subspace can be readily searched to correct aberrations via a deformable mirror. We demonstrate improved image quality when imaging a neural tissue, the mouse vomeronasal organ.

2. A homogeneous planar tissue model

Consider a sample which has an index of refraction n_s different from the immersion index n_i so that $n_s = n_i + \varepsilon$. Here we will focus in particular on the case where the surface is planar (Fig. 1), appropriate for flat or large samples where the local curvature is small compared to the field of view. In this case, the points at the tissue surface satisfy $\mathbf{x} \cdot \hat{\mathbf{n}} = c$, where $\hat{\mathbf{n}}$ is the unit normal and c is a constant.

Starting from an object point $\mathbf{x}_0$, a ray propagating in a direction $\hat{\mathbf{e}}$ intersects the surface after traveling a distance $s(\hat{\mathbf{e}})$, where for a flat surface we have

$$s(\hat{\mathbf{e}}) = \frac{c - \mathbf{x}_0 \cdot \hat{\mathbf{n}}}{\hat{\mathbf{e}} \cdot \hat{\mathbf{n}}}. \tag{1}$$

The numerator is recognized as the perpendicular distance $d_\perp$ to the tissue surface.

In the appendix, we show that to lowest order in ε the aberrations can be calculated in terms of the excess path length experienced by "unperturbed" rays. For the ray described in Eq. (1), the excess path length is simply $\varepsilon s(\hat{\mathbf{e}})$.

#189627 - $15.00 USD Received 29 Apr 2013; revised 20 Jun 2013; accepted 30 Jun 2013; published 14 Aug 2013

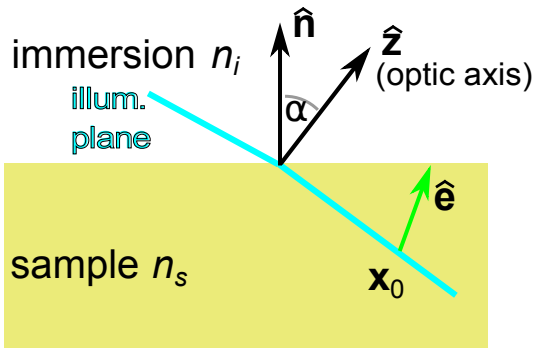

Fig. 1. Geometry of light-sheet imaging for extended samples. The sample is modeled as a flat interface, with the light sheet (cyan) entering at an angle. Emitted fluorescence from sample point $\mathbf{x_0}$ (green ray) is shown, propagating in the direction $\hat{\mathbf{e}}$. The tissue normal $\hat{\mathbf{n}}$ is at an angle α relative to the optic axis $\hat{\mathbf{z}}$. The sample has refractive index n_s and the immersion fluid n_i.

3. Defocus in meridional planes

To illustrate our approach, we begin with a relatively simple calculation of the lowest-order aberration, defocus, for a thin pencil of rays centered around the optic axis $\hat{\mathbf{z}}$. The defocus can be calculated by modeling each ray's excess path length as if the pencil originates from a shifted source point $\mathbf{x}_0 + \Delta\mathbf{x}$. We therefore seek a $\Delta\mathbf{x}$ satisfying

$$|\mathbf{x} - \mathbf{x}_0| + \varepsilon s(\hat{\mathbf{e}}) \approx |\mathbf{x} - (\mathbf{x}_0 + \Delta\mathbf{x})| + C \tag{2}$$

over the pencil of rays. The constant C is allowed because a ray-independent shift of the optical path length has no physical consequence. If we expand the right hand side for small $\Delta\mathbf{x}$, we obtain

$$\varepsilon s(\hat{\mathbf{e}}) \approx C - \hat{\mathbf{e}} \cdot \Delta\mathbf{x}. \tag{3}$$

First consider the meridional plane spanned by $\hat{\mathbf{z}}$ and $\hat{\mathbf{n}}$ (Fig. 1). In this plane, we can write $\hat{\mathbf{e}} = \cos\theta\hat{\mathbf{z}} + \sin\theta\hat{\mathbf{y}}$, where $\hat{\mathbf{y}}$ is the coordinate perpendicular to $\hat{\mathbf{z}}$ in this plane and is parallel to the direction of propagation of the illumination. If the angle between the tissue normal and the optic axis is α, then $\hat{\mathbf{z}} \cdot \hat{\mathbf{n}} = \cos\alpha$ and $\hat{\mathbf{y}} \cdot \hat{\mathbf{n}} = \sin\alpha$. Thus

$$s = \frac{d_\perp}{\cos\theta\cos\alpha + \sin\theta\sin\alpha} \tag{4}$$

$$\approx \frac{d_\perp}{(1-\theta^2/2)\cos\alpha + \theta\sin\alpha} \tag{5}$$

$$\approx \frac{d_\perp}{\cos\alpha}\left[1 - \theta\tan\alpha + \frac{1}{2}\theta^2\left(1 + 2\tan^2\alpha\right)\right] \tag{6}$$

for small θ. We recognize $d_\perp/\cos\alpha$ as d_z, the depth measured along the optic axis.

Substituting this parametrization into Eq. (3), we obtain

$$\Delta y = \varepsilon d_z \tan\alpha, \qquad \Delta z = \varepsilon d_z(1 + 2\tan^2\alpha). \tag{7}$$

This matches results obtained previously by ray tracing [10] for small ε. It is possible to correct this defocus with a small tilt of the light sheet [10].

#189627 - $15.00 USD Received 29 Apr 2013; revised 20 Jun 2013; accepted 30 Jun 2013; published 14 Aug 2013

One can also treat the other meridional plane, for which we let $\hat{\mathbf{e}} = \cos\theta\hat{\mathbf{z}} + \sin\theta\hat{\mathbf{x}}$, where $\hat{\mathbf{x}}\cdot\hat{\mathbf{n}} = 0$. Then

$$s = \frac{d_\perp}{\cos\theta\cos\alpha} \tag{8}$$

$$\approx \frac{d_\perp}{\cos\alpha}\left[1+\frac{1}{2}\theta^2\right]. \tag{9}$$

From Eq. (3) one obtains

$$\Delta x = 0, \qquad \Delta z = \varepsilon d_z. \tag{10}$$

Comparing Eq. (7) and Eq. (10), we see that the shift Δz is different in the two meridional planes, so the defocus is anisotropic. The mean defocus along $\hat{\mathbf{z}}$ is

$$\overline{\Delta z} = \varepsilon d_z(1+\tan^2\alpha). \tag{11}$$

In the special case $\alpha = 0$, this corresponds to the well-known result that the apparent depth of a source point is smaller (for $n_s > n_i$) than the real depth, $d_{\text{apparent}} = (n_i/n_s)d_{\text{real}}$. (Note that this special case is the only one for which the defocus is isotropic.)

This result also indicates a significant opportunity for improvement using adaptive optics. The maximum extent of the defocus anisotropy is $2\varepsilon d_z\tan^2\alpha$. For $\varepsilon = 0.03$, $\alpha = 45^\circ$, and $d_z = 200\mu$m, the difference between the two Δz results is 12μm, significantly larger than the typical z-thickness of the light sheet.

4. General aberrations from a homogeneous tissue model

To compute aberrations over an extended field of view, we convert the displacement $\mathbf{x}_0$ of the source point and the direction $\hat{\mathbf{e}}$ of each ray into coordinates in the back pupil plane [11]. Let the objective's focal length be f_0, and for a three-dimensional vector $\mathbf{w}$ consider just the two-dimensional projection $\mathbf{w}_\perp$ in the plane perpendicular to the optic axis. In such coordinates, for a lens satisfying the sine condition [12] we may write $\mathbf{x}_{0\perp}$ and $\mathbf{e}_\perp$ in terms of new variables $\mathbf{u}$ and $\mathbf{v}$, where $\mathbf{x}_{0\perp} = -f_0\mathbf{u}$ and $\mathbf{e}_\perp = a\mathbf{v}-\mathbf{u}$, where $a = |R/f_0|$ is the radius R of the back aperture scaled by f_0. The back-aperture position coordinate $\mathbf{v}$ assumes values over the entire unit circle.

In these coordinates, the wavefront aberration of Eq. (1) is written

$$\Phi(\mathbf{v},\mathbf{u}) = \frac{\varepsilon d_\perp}{\cos\alpha\sqrt{1-(a\mathbf{v}-\mathbf{u})^2}+\sin\alpha(av_y-u_y)} \tag{12}$$

$$= \frac{\varepsilon d_z}{\sqrt{1-(a\mathbf{v}-\mathbf{u})^2}+\tan\alpha(av_y-u_y)} \tag{13}$$

For the idealized model of Fig. 1 where the index mismatch is known, this expression has no free parameters and hence provides a mechanism to correct aberrations without any need for wavefront sensing or optimization. In practice, often one will not know ε for the specific tissue under investigation, and likewise the sample may be slightly tilted so that even α may not be known exactly. As a consequence, it is worth considering the two dimensional family of solutions

$$\Phi(\mathbf{v},\mathbf{u}) = \frac{A}{\sqrt{1-(a\mathbf{v}-\mathbf{u})^2}+t(av_y-u_y)}. \tag{14}$$

Here we have defined $t = \tan\alpha$ for convenience; both A and t would be regarded as fitting parameters.

#189627 - $15.00 USD Received 29 Apr 2013; revised 20 Jun 2013; accepted 30 Jun 2013; published 14 Aug 2013

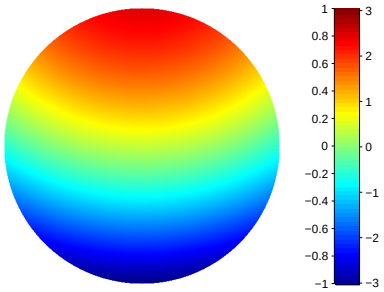

Fig. 2. Back pupil correction, Eq. (15), for $a = 0.37$, a tilt angle $\alpha = 30^\circ$, and $\beta = c_2^0$, Eq. (19). The colorbar is scaled in relative units (left) and in μm of wavefront aberration (right) for the specific case of $\varepsilon = 0.04$ and $d_z = 100\,\mu$m.

Eq. (14) can be used directly to specify the shape of a deformable mirror to correct the aberrations. (Because A is depth-dependent, this correction can only be done for a "stripe" of constant depth within the sample.) For example, for the center of the field of view ($\mathbf{u} = 0$), the mirror should be tuned to assume a shape

$$-\frac{1}{2}\Phi(\mathbf{v},0) = A'\left[\frac{1}{\sqrt{1-a^2\mathbf{v}^2}+tav_y} - c_0^0 - 2c_1^{-1}v_y - \beta(2\mathbf{v}^2-1)\right]. \tag{15}$$

Here, the coefficients c are the Zernike coefficients, calculated below. Because piston, tip, and tilt do not affect image quality these are subtracted (note tip is already zero); we have also introduced a third parameter, β, for defocus, as the best focus of the light sheet can be difficult to determine in the presence of higher-order aberrations. For microscopy, the normalized coordinate $\mathbf{u}$ is in practice quite small: $|\mathbf{u}| < 0.04$, whereas $a = 0.37$ for a water-immersion objective with NA 0.5. As a consequence, this solution may suffice (at a particular depth within the tissue) over the field of view. This aberration is shown in Fig. 2, for the case $\beta = c_2^0$ (meaning that the sheet is already in focus).

In many cases, the deformable mirror may have been calibrated using a Zernike basis. As a consequence, it is useful to calculate the projections of $\Phi(\mathbf{v},0)/A$ onto such a basis, so that the mirror shape parametrized by Φ can be represented in terms of Zernike coefficients. For an object in the center of the field of view, up to fourth order these are:

$$c_0^0 = \frac{1}{8}\left(a^4t^4 + 2a^4t^2 + 2a^2t^2 + a^4 + 2a^2 + 8\right); \tag{16}$$

$$c_1^{-1} = -\frac{at(3a^2t^2 + 4a^2 + 6)}{3}; \tag{17}$$

$$c_1^1 = 0; \tag{18}$$

$$c_2^0/\sqrt{3} = \frac{a^2(t^2+1)(3a^2t^2 + 3a^2 + 4)}{16}; \tag{19}$$

$$c_2^{-2}/\sqrt{6} = 0; \tag{20}$$

$$c_2^2/\sqrt{6} = -\frac{a^2t^2(6a^2t^2 + 9a^2 + 8)}{16}; \tag{21}$$

#189627 - $15.00 USD Received 29 Apr 2013; revised 20 Jun 2013; accepted 30 Jun 2013; published 14 Aug 2013

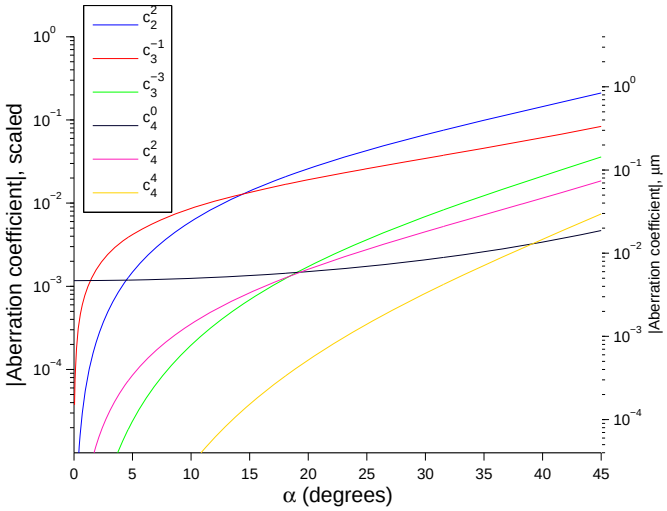

Fig. 3. Magnitude of aberration coefficients, Eqs. (21–30), as a function of the tilt angle α. The coefficients are displayed in units of $A = \varepsilon d_z$ (left) and in μm of wavefront aberration (right) for the same parameters used in Fig. 2.

$$c_3^{-1}/\sqrt{8} = -\frac{a^3 t(3t^2+4)}{12}; \tag{22}$$

$$c_3^{1}/\sqrt{8} = 0; \tag{23}$$

$$c_3^{-3}/\sqrt{8} = \frac{a^3 t^3}{4}; \tag{24}$$

$$c_3^{3}/\sqrt{8} = 0; \tag{25}$$

$$c_4^{0}/\sqrt{5} = \frac{a^4(t^2+1)^2}{16}; \tag{26}$$

$$c_4^{-2}/\sqrt{10} = 0; \tag{27}$$

$$c_4^{2}/\sqrt{10} = -\frac{a^4 t^2(2t^2+3)}{16}; \tag{28}$$

$$c_4^{-4}/\sqrt{10} = 0; \tag{29}$$

$$c_4^{4}/\sqrt{10} = \frac{a^4 t^4}{8}. \tag{30}$$

These are plotted as a function of tilt angle in Fig. 3.

The number of parameters in this representation of the aberration is so low that no particular specialized procedures are required to perform aberration correction. Indeed, setting these parameters can easily be performed in the same way that microscopes are usually focused: visual tuning by the user. Naturally, this does not preclude more algorithmically-based approaches, but a key advantage of the analytic representation of Eq. (15) is that it greatly reduces the demands on all other components of the adaptive optics system.

5. Experimental results

An Objective-Coupled Planar Illumination (OCPI) microscope with adaptive-optics correction was built and calibrated as described [13]. The mirror shape was parametrized in the Zernike

#189627 - $15.00 USD Received 29 Apr 2013; revised 20 Jun 2013; accepted 30 Jun 2013; published 14 Aug 2013

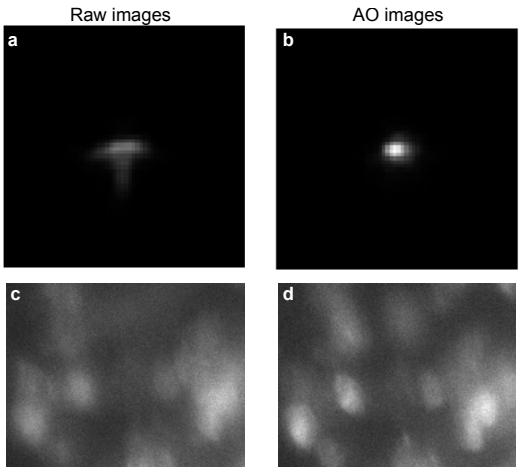

Fig. 4. Aberration correction in OCPI microscopy. (**a**) A 0.2 μm bead in PDMS, $d_z = 80\,\mu$m. (**b**) The same bead after aberration correction. (**c**) Neurons of the vomeronasal organ in a mouse expressing GCaMP2, $d_z = 50\,\mu$m. (**d**) The same field as (c) after correction.

basis described in section 4, using A', t, and β as tunable coefficients. We found that in practice the user could tune these coefficients to a reasonable optimum with fewer than 20 images collected during tuning. These settings sufficed for imaging the same region of tissue over tens of minutes.

Figure 4 shows the improvement in image quality from this procedure, using two samples. In Fig. 4(a), a 200 nm bead is visualized in polydimethylsiloxane (PDMS, Dow Corning, DC 184-A and DC 184-B with a weight ratio of 10:1, $n = 1.40$). Figure 4(b) shows the corrected image on the same intensity scale; the peak intensity is increased by slightly over two-fold, and the bead image is considerably more compact. Figure 4(c) shows an image of GCaMP2-expressing neurons in the vomeronasal organ of a mouse [14]; the corrected version is seen in Fig. 4(d). It is apparent that many details of the image are considerably improved. AO correction resulted in overall 18% increase in the r.m.s. pixel intensity, and a 20% increase in the peak intensity.

6. Conclusion

Here we demonstrate a simple procedure for improving image quality in light sheet microscopy. For extended samples with a flat interface, the lowest-order aberrations may be calculated directly using a simple tissue model. This model greatly reduces the complexity of adaptive optics, by providing a functional form of the aberrations containing only two or three free parameters. These parameters are readily tuned at the beginning of image collection, and the corrected images show considerably improved quality. We believe that this represents a promising and pragmatic approach for many applications of light sheet microscopy.

A. Optical path length: a perturbative approach

Optical propagation through a sample can be expressed in terms of the optical path length (also known as the point characteristic [11]),

$$\zeta(\mathbf{x}_0, \mathbf{x}_1) = \inf_C S[C]\,, \tag{31}$$

#189627 - $15.00 USD Received 29 Apr 2013; revised 20 Jun 2013; accepted 30 Jun 2013; published 14 Aug 2013

where C is a curve $\mathbf{x}(s)$ running from $\mathbf{x}_0$ to $\mathbf{x}_1$ and

$$S[C] = \int \mathrm{d}s\, L = \int \mathrm{d}s\, n(\mathbf{x}(s))|\dot{\mathbf{x}}(s)|. \tag{32}$$

Here $n(\mathbf{x})$ is the index of refraction at position $\mathbf{x}$.

Consider an aberration that arises as a small perturbation $\varepsilon(\mathbf{x})$ of the index of refraction, i.e., $n(\mathbf{x}) \Rightarrow n(\mathbf{x}) + \varepsilon(\mathbf{x})$ so that

$$\zeta_{\mathrm{tot}}(\mathbf{x}_0, \mathbf{x}_1) = \inf_C S_{\mathrm{tot}} = \inf_C (S_n + S_\varepsilon), \tag{33}$$

where S_n is given by Eq. (32) and S_ε is of the same form, with $n(\mathbf{x}(s))$ replaced by $\varepsilon(\mathbf{x}(s))$. We want to expand ζ_{tot} to lowest order in ε.

Consider the curve $C_\star$ that satisfies $\inf_C S_n[C]$. We'll expand S around $C_\star$ as $C = C_\star + \delta C$. We have

$$\begin{aligned} S_{\mathrm{tot}}[C_\star + \delta C] &= S_n[C_\star + \delta C] + S_\varepsilon[C_\star + \delta C] &(34)\\ &\approx S_n[C_\star] + \frac{1}{2}\int S_n''[C_\star]\delta C^2 + S_\varepsilon[C_\star] + \int S_\varepsilon'[C_\star]\delta C + \frac{1}{2}\int S_\varepsilon''[C_\star]\delta C^2. &(35)\end{aligned}$$

We note in particular that the $S_n'[C_\star]$ term is zero because $C_\star$ is an extremum of S_n. The integrand is a sum of the form

$$L_{\mathrm{tot}}(C_\star + \delta C) \approx L_{\mathrm{tot}}(C_\star) + b\delta C + a\delta C^2. \tag{36}$$

Note that b is of first order in ε, because it represents the $S_\varepsilon'[C_\star]$ term in Eq. (35). In contrast, a is zeroth-order in ε because it includes the $S_n''[C_\star]$ term in Eq. (35). (If $S_n''[C_\star] = 0$, which can happen for certain δC if $\mathbf{x}_0$ and $\mathbf{x}_1$ are conjugate points in an imaging system, then a too is first order in ε, but we will be careful not to use these expressions in such a case.) δC thus satisfies $\delta C = -b/2a$, and thus

$$L_{\mathrm{tot}}(C_\star + \delta C) \approx L_{\mathrm{tot}}(C_\star) - \frac{b^2}{2a}. \tag{37}$$

Thus, the corrected path contributes to Eq. (37) only in second order in ε. Therefore, to first order the optical path length under a small perturbation is just

$$\zeta_{\mathrm{tot}} = S_n[C_\star] + S_\varepsilon[C_\star]. \tag{38}$$

This makes it straightforward to evaluate the effect of a small perturbation.

Acknowledgments

This work was funded by NIH NINDS/NIAAA (R01 NS068409, TEH) and a McKnight Technological Innovation Award in Neuroscience (TEH).

#189627 - $15.00 USD Received 29 Apr 2013; revised 20 Jun 2013; accepted 30 Jun 2013; published 14 Aug 2013